

ACCEPTED MANUSCRIPT

## Alternative stacking sequences in hexagonal boron nitride

To cite this article before publication: Stephen Matthew Gilbert *et al* 2019 *2D Mater.* in press <https://doi.org/10.1088/2053-1583/ab0e24>

### Manuscript version: Accepted Manuscript

Accepted Manuscript is "the version of the article accepted for publication including all changes made as a result of the peer review process, and which may also include the addition to the article by IOP Publishing of a header, an article ID, a cover sheet and/or an 'Accepted Manuscript' watermark, but excluding any other editing, typesetting or other changes made by IOP Publishing and/or its licensors"

This Accepted Manuscript is © 2019 IOP Publishing Ltd.

During the embargo period (the 12 month period from the publication of the Version of Record of this article), the Accepted Manuscript is fully protected by copyright and cannot be reused or reposted elsewhere.

As the Version of Record of this article is going to be / has been published on a subscription basis, this Accepted Manuscript is available for reuse under a CC BY-NC-ND 3.0 licence after the 12 month embargo period.

After the embargo period, everyone is permitted to use copy and redistribute this article for non-commercial purposes only, provided that they adhere to all the terms of the licence <https://creativecommons.org/licenses/by-nc-nd/3.0>

Although reasonable endeavours have been taken to obtain all necessary permissions from third parties to include their copyrighted content within this article, their full citation and copyright line may not be present in this Accepted Manuscript version. Before using any content from this article, please refer to the Version of Record on IOPscience once published for full citation and copyright details, as permissions will likely be required. All third party content is fully copyright protected, unless specifically stated otherwise in the figure caption in the Version of Record.

View the [article online](#) for updates and enhancements.

## Alternative Stacking Sequences in Hexagonal Boron Nitride

S. Matt Gilbert<sup>1,2,3</sup>, Thang Pham<sup>1,2,3,4</sup>, Mehmet Dogan<sup>1,2</sup>, Sehoon Oh<sup>1,2</sup>, Brian Shevitski<sup>1,2,3,5</sup>, Gabe Schumm<sup>1,2,3</sup>, Stanley Liu<sup>1,2,3</sup>, Peter Ercius<sup>5</sup>, Shaul Aloni<sup>5</sup>, Marvin L. Cohen<sup>1,2</sup>, and Alex Zettl<sup>1,2,3,\*</sup>

<sup>1</sup> Department of Physics, University of California at Berkeley, Berkeley, CA 94720, USA

<sup>2</sup> Materials Sciences Division, Lawrence Berkeley National Laboratory, Berkeley, CA 94720, USA

<sup>3</sup> Kavli Energy NanoScience Institute at the University of California, Berkeley and the Lawrence Berkeley National Laboratory, Berkeley, CA 94720, USA

<sup>4</sup> Department of Materials Science and Engineering, University of California at Berkeley, Berkeley, CA 94720, USA

<sup>5</sup> Molecular Foundry, Lawrence Berkeley National Laboratory, Berkeley, CA 94720, USA

\*Corresponding author: azettl@berkeley.edu

### Abstract:

The relative orientation of successive sheets, i.e. the stacking sequence, in layered two-dimensional materials is central to the electronic, thermal, and mechanical properties of the material. Often different stacking sequences have comparable cohesive energy, leading to alternative stable crystal structures. Here we theoretically and experimentally explore different stacking sequences in the van der Waals bonded material hexagonal boron nitride (h-BN). We examine the total energy, electronic bandgap, and dielectric response tensor for five distinct high symmetry stacking sequences for both bulk and bilayer forms of h-BN. Two sequences, the generally assumed AA' sequence and the relatively unknown (for h-BN) AB (Bernal) sequence, are predicted to have comparably low energy. We present a scalable modified chemical vapor deposition method that produces large flakes of virtually pure AB stacked h-BN; this new material complements the generally available AA' stacked h-BN.

### Introduction

1  
2  
3 In recent years there has been a dramatic resurgence in interest in van der Waals  
4 bonded layered materials, including graphite, boron-nitride, and transition metal  
5  
6 bonded layered materials, including graphite, boron-nitride, and transition metal  
7  
8 dichalcogenides.<sup>1,2</sup> These materials display strong intraplane (typically covalent) bonding  
9  
10 and weak van der Waals interplane bonding, which facilitates exfoliation into mono-layer  
11  
12 or few-layer forms, and further allows custom stack-ups or laminations of sheets with  
13  
14 different chemical composition or crystallographic orientation.<sup>1-8</sup> Even for a material  
15  
16 composed of identical sheets, the stacking order of the successive sheets or layers, which  
17  
18 may be translationally and/or rotationally shifted, can profoundly influence the overall  
19  
20 physical properties.<sup>9-12</sup> For example, for naturally occurring graphite the usual stacking  
21  
22 sequence is Bernal (AB) stacking, but rhombohedral (ABC) stacking is also possible,  
23  
24 which has a completely different electronic band structure.<sup>13,14</sup>  
25  
26  
27

28  
29 Hexagonal boron nitride (h-BN) is structurally very similar to graphite, with  
30  
31 successively stacked (and van der Waals bonded) sheets of hexagonally arranged  $sp^2$ -  
32  
33 bonded boron and nitrogen.<sup>5</sup> However, unlike graphite, h-BN is purely synthetic, with a  
34  
35 wide electronic band gap (hence the nickname "white graphite").<sup>15-17</sup> Virtually all  
36  
37 synthesis methods for h-BN lead to an AA' stacking sequence, where atoms in one layer  
38  
39 all lie directly above atoms in the next layer.<sup>4,18-20</sup> Successive layers are rotated such that  
40  
41 all nitrogens lie above borons, and all borons lie above nitrogens.<sup>20</sup> Potential alternative  
42  
43 stacking sequences for h-BN are of great theoretical and experimental interest.  
44  
45  
46

47 Here we explore these alternative h-BN stacking sequences. We employ Density  
48  
49 Functional Theory (DFT) to determine the total energy, electronic band structure, and  
50  
51 dielectric tensor elements for five different high-symmetry h-BN stackings. We find that  
52  
53 Bernal (AB) stacked h-BN has a total energy comparable to, and indeed a bit lower than,  
54  
55  
56  
57  
58  
59  
60

1  
2  
3 that for conventional AA' stacked h-BN. This suggests that Bernal stacked h-BN should  
4 be stable. We present a modified Low-Pressure Chemical Vapor Deposition (LP-CVD)  
5 method that reliably produces large flakes of few-layer Bernal stacked h-BN. This new  
6 form of h-BN is characterized by electron diffraction and atomic-resolution transmission  
7 electron microscopy measurements.  
8  
9  
10  
11  
12  
13  
14  
15  
16

### 17 **h-BN Stacking Sequences**

18  
19 Fig. 1 schematically shows five high-symmetry stacking sequence possibilities for  
20 h-BN. Boron and nitrogen atoms are indicated in gold and blue, respectively. In each  
21 schematic, only two superposed atomic sheets or layers are shown, and for visual clarity  
22 atoms in the top layer have been drawn slightly smaller than atoms in the bottom layer.  
23  
24 Because there is no nomenclature consensus in the literature for all of these stacking  
25 sequences, we here adopt a naming convention where “prime” denotes a  $60^\circ$  rotation, and  
26 the letters A and B are used in the standard way as for graphite.  
27  
28  
29  
30  
31  
32  
33  
34

35 AA is the simplest stacking sequence; here the atoms in consecutive layers  
36 exactly align (B on B, and N on N). AA' is obtained from AA by rotating every other  
37 layer by  $60^\circ$  and aligning the hexagons (B on N). AB is obtained from AA by shifting  
38 every other layer, as demonstrated by the red arrow in the upper right panel of the figure,  
39 which yields a structure where half of the B atoms align with half of the N atoms, and the  
40 remaining half of the atoms align with the centers of the hexagons in the neighboring  
41 layers. Shifting every second layer in AA', as demonstrated by the red arrows in the  
42 lower right two panels of Fig. 1, yields AB1' and AB2'. In AB1' (AB2'), all the B (N)  
43 atoms are aligned, and all the N (B) atoms align with the centers of the hexagons in the  
44  
45  
46  
47  
48  
49  
50  
51  
52  
53  
54  
55  
56  
57  
58  
59  
60

1  
2  
3 neighboring layers. Applying to AA the lateral shift that we use to obtain AB2' from AA'  
4 yields an equivalent structure to AB; therefore, there are a total of five physically distinct  
5  
6  
7 structures that preserve the three-fold symmetry. We reiterate that AB stacking, also  
8  
9 called Bernal stacking, is the stacking sequence most prevalent in naturally-occurring  
10  
11  
12 crystalline graphite,<sup>21</sup> while virtually all h-BN produced today and used in laboratories  
13  
14  
15 worldwide has the stacking sequence AA'.<sup>4,15,18,20</sup>  
16  
17

### 18 19 **Theoretical Results**

20  
21 Using density functional theory (DFT), we explore the total cohesive energy,  
22  
23  
24  
25  
26  
27  
28  
29  
30  
31  
32  
33  
34  
35  
36  
37  
38  
39  
40  
41  
42  
43  
44  
45  
46  
47  
48  
49  
50  
51  
52  
53  
54  
55  
56  
57  
58  
59  
60

Using density functional theory (DFT), we explore the total cohesive energy, electronic band structure, and dielectric response tensor for the infinite crystal (bulk) and bilayer forms of h-BN, in the five physically distinct stacking sequences presented in Fig. 1. Similar calculations for total energy and band structure have been published previously by various other groups; unfortunately since the results are highly sensitive to the computational details such as the exchange-correlation functional and the van der Waals scheme, they yield inconsistencies.<sup>22-27</sup>

Table A presents the total energies of bulk and bilayer h-BN in the different stacking sequences, as computed in DFT. We take the AA' stacking to be the reference and set its energy to zero. We also include the results from previous studies for comparison. We find AB to be the ground state (i.e. it has the lowest overall energy) for both bulk and bilayer BN. However, AA' is quite close in energy (3 meV per unit cell higher for bulk). AB1' is next closest in energy (8 meV per unit cell higher for bulk). This hierarchy is consistent with some reports in the literature<sup>24,27</sup> but at odds with others<sup>22,25</sup>. We also find that AA and AB2', while close to each other in energy, are significantly

1  
2  
3 higher in energy than the other three stackings. This can be understood by simple  
4 arguments such as those suggested in Ref. 11. Aligning negatively charged nitrogen  
5 atoms with large electron clouds causes a repulsive Pauli interaction between the layers,  
6 increasing the total energies and the interlayer distances to 3.64 Å for AA and 3.54 Å for  
7 AB2' (from 3.33 Å for AA', AB and AB1'). We note that these two high-energy stackings  
8 are also energetically unstable, i.e. they do not correspond to local energy minima in the  
9 configuration landscape and relax to one of the stable configurations when the atoms are  
10 slightly perturbed.  
11  
12  
13  
14  
15  
16  
17  
18  
19  
20  
21

22 Fig. 2 shows our band structure results for h-BN bilayers (assumed suspended in  
23 vacuum). The zeros of the energy levels are set to the vacuum level for each structure so  
24 that there is a common reference between the plots. For additional insight we have  
25 projected the Kohn-Sham wavefunctions onto the atomic orbitals for each point along the  
26 bands we have computed. The resulting atomic orbital characteristics are designated by  
27 red (blue) coloring for boron (nitrogen) n=2 (2s & 2p) orbitals. We observe that the top of  
28 the valence band mostly consists of nitrogen n=2 orbitals, and the bottom of the  
29 conduction band mostly consists of boron n=2 orbitals, which verifies the ionic character  
30 of the intralayer bonds in h-BN, and is consistent with a large-gap insulator.  
31  
32  
33  
34  
35  
36  
37  
38  
39  
40  
41

42 We summarize the band gaps we have obtained for h-BN in its bulk and bilayer  
43 forms in Table B. Due to the underestimation of band gaps in DFT, the values tabulated  
44 are expected to be much lower than experimental measurements, which are in the 4 to 7  
45 eV range.<sup>22</sup> However, the relative values of the computed gaps can be expected to be  
46 mostly accurate. For instance, in Refs. 28 and 24, the bandgaps are computed with and  
47 without a GW correction, respectively, and it is found that the GW correction adds about  
48  
49  
50  
51  
52  
53  
54  
55  
56  
57  
58  
59  
60

1  
2  
3 1.6 eV to the value of each gap. We also expect the shapes of the bands to be correctly  
4 predicted by DFT; therefore, the predictions as to whether a band gap is direct or indirect  
5 are reliable. We find that both AA' and AB have indirect gaps. However, the AB  
6 structure allows an optical transition at the K point with an energy only 1% larger than  
7 the band gap. This is a key feature distinguishing the electronic structure of AB stacking  
8 from AA' stacking in h-BN.  
9

10  
11  
12  
13  
14  
15  
16  
17 Table C summarizes our calculations for the dielectric tensor of bilayer and bulk  
18 h-BN, for the five selected stacking sequences. Because of the high symmetry of h-BN,  
19 the dielectric tensor only has two distinct non-zero values: the in-plane  $\epsilon_{xx}=\epsilon_{yy}$  (which we  
20 denote as  $\epsilon_{||}$ ), and the out-of-plane  $\epsilon_{zz}$  (which we denote as  $\epsilon_{\perp}$ ). We compute the dielectric  
21 tensor in two frequency limits:  $\epsilon_{\infty}$  and  $\epsilon_0$ , for high and low frequency, respectively. In the  
22 Born-Oppenheimer approximation, for high-frequency electric field response, the nuclei  
23 can be thought of as stationary, and the electronic response dominates. In this case, the  
24 dielectric response is described by  $\epsilon_{\infty}$ , which we compute via the density functional  
25 perturbation theory.<sup>29</sup> For low-frequency electric-field response,  $\epsilon_0$ , we compute the  
26 relaxed-ion dielectric tensor, following the methodology proposed by Ref. 30.  
27  
28  
29  
30  
31  
32  
33  
34  
35  
36  
37  
38  
39

40 We find that the dielectric tensor values for AA', AB and AB1' are very close, and  
41 larger than the values for AA and AB2' by 0.2 to 0.4. This simple trend can be  
42 understood as a result of the difference in the interlayer distance between these two  
43 groups of stackings. In the former group, which has smaller interlayer distances, the  
44 dielectric material simply occupies a larger portion of the space, leading to a larger  
45 dielectric tensor. Our results for the relaxed-ion tensors indicate that the response of the  
46 nuclei to a finite electric field does not significantly depend on the stacking, further  
47  
48  
49  
50  
51  
52  
53  
54  
55  
56  
57  
58  
59  
60

1  
2  
3 emphasizing the weakness of the interlayer ionic interactions. We have also compared  
4  
5 our results with Ref. 31 for the AA' stacking, which, to our knowledge, is the only  
6  
7 available calculation of these values in the literature. Our results are in good agreement  
8  
9 for the in-plane dielectric constant values, and in reasonable agreement for the out-of-  
10  
11 plane values. For the  $\epsilon$  values in the bilayer case, we have carefully corrected for the  
12  
13 existence of vacuum in our simulations by applying the combined capacitor rules, as  
14  
15 described in Ref. 31. For the slab thickness we have used twice the value of the interlayer  
16  
17 distance in each stacking.  
18  
19

### 20 21 **Motivation for Experiment**

22  
23 The total energy calculation results presented in Table A suggest that of the 5 high  
24  
25 symmetry stacking sequences of h-BN, AA and AB2' structures are likely highly  
26  
27 unstable. The remaining three sequences, AA', AB, and AB1' are relatively close in  
28  
29 energy, with AB representing the ground state. The original synthesis of h-BN by  
30  
31 Balmain in 1842<sup>32,33</sup> yielded material with AA' stacking, and this situation continues  
32  
33 today: virtually all h-BN produced by all synthetic routes has the AA' stacking sequence.  
34  
35 This begs the question, is a synthesis route possible that allows access to the distinct AB  
36  
37 Bernal ground state structure, or possibly the slightly higher energy AB1' configuration?  
38  
39

40  
41 Apart from the properties discussed above, AB Bernal-stacked h-BN has been  
42  
43 predicted to possess a tunable bandgap, along with other unique optical features.<sup>34-36</sup>  
44  
45 Previous experimental studies have observed tantalizing small pockets of AB-stacked  
46  
47 bilayer h-BN.<sup>35,37-39</sup> Therefore, we are motivated to develop a viable synthetic route for  
48  
49 the reliable synthesis of AB-stacked h-BN, a new form of two-dimensional insulator.  
50  
51  
52  
53  
54  
55  
56  
57  
58  
59  
60



## Experimental Results

We employ Low-Pressure Chemical Vapor Deposition (LP-CVD) on a transition metal surface to select the stacking growth sequence of h-BN. We find that the growth can be tuned from conventional AA' growth to exclusively Bernal AB growth, on both Cu and Fe substrates. High-Resolution Transmission Electron Microscopy (HRTEM) and Selected Area Electron Diffraction (SAED) are used to reveal the Bernal-stacking of the resulting multilayer flakes.

Fig. S1 shows the furnace setup used for the synthesis. Similar to Ref. 17 and our previous work<sup>40,41</sup>, we employ a two-zone heating approach in which the gaseous thermal decomposition products of solid ammonia-borane (heated at 70-90 °C in region T<sub>0</sub> in Fig. S1) react to form h-BN on a transition metal catalyst (heated at at 1025 °C in region T<sub>1</sub> in Fig. S1). Our synthesis method for Bernal-stacked h-BN differs from previous ammonia-borane based LP-CVD growths of h-BN in its combination of relatively low precursor temperatures (75-85 °C) and high hydrogen gas flows (100-200 sccm).<sup>17,42-44</sup> Additional details on the growth are available in the supplementary methods section.

Figs. 3a-b show two representative Scanning Electron Microscope (SEM) images of few-layer h-BN flakes grown on Fe via the LP-CVD method (30 min, 100 sccm H<sub>2</sub>). The concentric triangular shape and 40+ μm size of the flakes are representative of those grown over much of the entire metal substrate, with an average total substrate coverage by h-BN of approximately 50-90% depending on the growth conditions.

The stacking sequence of the h-BN flakes is examined by SAED and HRTEM. SAED has been demonstrated as an effective means to characterize the stacking of graphene.<sup>45-47</sup> By comparing the intensity of the first-order ((±100), (0±10), and

1  
2  
3  $(\pm 1 \mp 10)$  and second-order  $((\pm 2 \mp 10), (0 \pm 10), \text{ and } (\pm 1 \mp 20))$  diffraction peaks, the  
4  
5 stacking of the layers can be deduced.  
6  
7

8 Fig. 3c shows an SAED pattern of an h-BN flake originally grown via LP-CVD  
9 on an Fe substrate. The ratio of the intensities of the first-order  $\langle 010 \rangle$  and second-order  
10  $\langle 110 \rangle$  diffraction peaks is  $\sim 0.3$  (Fig. S2). We simulate the diffraction patterns of the  
11 stable bulk configurations of h-BN with AA' and AB stackings using the Single Crystal  
12 software package (as shown in Fig. S2) and compare with our measured values. Although  
13 ABC-stacked rhombohedral BN does not belong to the h-BN class, we also simulate the  
14 diffraction patterns for it to rule out this stacking in our material.<sup>48,49</sup> The experimental  
15 first-order to second-order ratio of  $\sim 0.3$  is consistent with the simulated ratio of 0.28 for  
16 AB stacked h-BN while the simulation of AA' yields a ratio of 1.1 and ABC yields a ratio  
17 of 0. These ratios of intensities are comparable to results in graphene.<sup>47</sup> This result  
18 indicates that the as grown h-BN is either AB, AB1', or AB2' stacked, as they possess  
19 similar intensity ratios.  
20  
21  
22  
23  
24  
25  
26  
27  
28  
29  
30  
31  
32  
33  
34

35 To differentiate between these stackings, we perform HRTEM on a bilayer region  
36 of material. Figs. 3d-e show aberration corrected HRTEM focal series reconstruction  
37 acquired at 80 kV (described in the methods section of the supplement) of two nearby  
38 mixed monolayer/bilayer regions of the multilayer h-BN as cropped from the full image  
39 shown in Fig. S3. The red dashed triangle denotes the boundary between the bilayer and  
40 monolayer/vacuum regions that were formed due to electron irradiation in the TEM.  
41  
42  
43  
44  
45  
46  
47  
48

49 The atomic positions in each region are deduced from Fig. 3d-e and are sketched  
50 in Fig. 3f. Based on the atomic positions as sketched, the two layers are AB stacked (see  
51 Fig. 1). We deduce the atomic positions shown in Fig. 3f by assuming that all edge-atoms  
52  
53  
54  
55  
56  
57  
58  
59  
60

1  
2  
3 of the triangular holes are N as is well-reported in the literature at ambient conditions.  
4  
5  
6<sup>20,40,50-53</sup> We thereby determine the position of all other atoms in both layers of the bilayer  
7  
8 area accordingly, as illustrated by the ball-and-stick model in Fig. 3f.  
9

10 We note that the monolayer regions in Figs. 3d,e are two different layers. The  
11  
12 regions shown in Fig 3d and 3e were close enough to be captured in the same HR-TEM  
13  
14 (Fig. S3) image allowing us to directly correlate their structures. The atoms of the  
15  
16 monolayer in Fig. 3d, which align with the referenced yellow line connecting bright  
17  
18 contrast spots running through the entire bilayer area (the bright contrast spots are  
19  
20 attributed to the overlapping of two atoms in the top and bottom layers), are all B. On the  
21  
22 other hand, the atoms of the monolayer, which also align with the referenced yellow line  
23  
24 as indicated in Fig. 3e, are all N. As the result, these monolayer regions reside in different  
25  
26 layers. More importantly, one layer translates with respect to the other by a single atomic  
27  
28 bond length ( $1.4 \text{ \AA}$ )<sup>20</sup> along the yellow reference line. This translation reflects AB  
29  
30 (Bernal) stacking as shown in Fig. 1. This is the first conclusive observation to our  
31  
32 knowledge of non-overlapping vacancies in two separate layers of a two-dimensional  
33  
34 material.  
35  
36  
37  
38  
39

40 The electron diffraction and HR-TEM results as shown in Fig. 3 are  
41  
42 representative across 100% of our samples grown on both iron and copper using this  
43  
44 synthesis process (except in regions where multiple flakes overlap at their edge resulting  
45  
46 in twisted multilayers at the interface). Moreover, we do not observe any high-symmetry  
47  
48 orientation other than AB stacking anywhere in our samples.  
49  
50  
51  
52  
53  
54  
55  
56  
57  
58  
59  
60

1  
2  
3 In order to elucidate the growth mechanism for Bernal-stacked h-BN, we explore  
4  
5 the role of this increase in hydrogen to elucidate the growth mechanism for Bernal-  
6  
7 stacked h-BN. Fig. 4a shows SEM images of four h-BN samples grown on Cu with  
8  
9 varying hydrogen gas flows (low 20 sccm, high 200 sccm) and growth time (20 min and  
10  
11 1 hour). In Fig. 4a(iii-iv), low hydrogen flows, when combined with low precursor  
12  
13 1 hour). In Fig. 4a(iii-iv), low hydrogen flows, when combined with low precursor  
14  
15 temperatures, lead to monolayer h-BN domains that merge into continuous films with  
16  
17 additional growth time. While some small regions of ad-layer h-BN are present (white  
18  
19 dots or triangles within the larger, darker h-BN monolayer triangle), the multilayer  
20  
21 regions do not appear to grow with increased times once the film fully covers the catalyst  
22  
23 (Fig. S4).  
24

25  
26 Conversely, for higher hydrogen flows the crystals quickly reach their final lateral  
27  
28 size and then ultimately do not merge into films as shown in Fig. 4a(i-ii). For short  
29  
30 growth times (20 min), the triangular h-BN domains grown with high hydrogen flow  
31  
32 (Fig. 4a(i)) are slightly smaller in comparison to those with low hydrogen flow (Fig.  
33  
34 4a(iii)), but these smaller crystals have a higher coverage of multilayered ad-layers. As  
35  
36 the growth time is increased, the h-BN crystals grown with high hydrogen-flow do not  
37  
38 significantly increase in size, but the size and coverage of multilayers increases as shown  
39  
40 in Fig. 4a(ii).  
41  
42

43  
44 We attribute the preference towards forming multilayer flakes rather than  
45  
46 continuous monolayer films to the etching properties of the hydrogen gas. Hydrogen gas  
47  
48 is known to etch the edges of h-BN domains at high temperatures.<sup>42,54</sup> Therefore, by  
49  
50 utilizing a high hydrogen flow as in Fig. 4a(iii-iv), the edges of the h-BN flakes are  
51  
52 etched throughout the growth, and the domains are prevented from merging into films  
53  
54  
55  
56  
57  
58  
59  
60

1  
2  
3 after reaching their equilibrium lateral size. While both the low and high hydrogen flow  
4 case lead to ad-layer formation, it appears their growth is halted once a continuous film  
5 has formed (Fig. S4).  
6  
7  
8  
9

10 Based on this observation, we propose an under-layer growth model for Bernal-  
11 stacked h-BN, as sketched in Fig. 4b. This type of mechanism has been previously  
12 described for multilayer graphene and h-BN.<sup>55-58</sup> In our LP-CVD process, low flows of  
13 precursor gas and high flows of hydrogen cause the edges of the h-BN domains to be  
14 continuously etched. This prevents the formation of a full coverage layer and allows the  
15 gaseous precursor to access the transition metal catalyst for the entire length of our  
16 procedure. The precursor gas can thereby adsorb onto or dissolve into the metal and form  
17 ad-layers below the first layer.  
18  
19  
20  
21  
22  
23  
24  
25  
26  
27

28 It has been previously reported that an h-BN layer grown on metal foil by CVD  
29 will have its orientation uniquely determined by the local configuration of the catalyst at  
30 the nucleation site of the h-BN.<sup>59</sup> Since each layer of h-BN grows directly on the catalyst  
31 in our process, its rotation can be controlled by the metal. Generally, we find that the  
32 layers of our Bernal-stacked h-BN grow as aligned triangles with a common centroid;  
33 this suggests the layers all form at a common nucleation point, forcing each layer to align  
34 to the metal. This mechanism results in aligned ( $0^\circ$  interlayer rotation) layers that relax  
35 into the AB ground state by interlayer sliding on the order of 1 Å at the elevated growth  
36 temperatures. This process also therefore excludes the stable AA' and AB1' stackings  
37 which have anti-aligned ( $60^\circ$  interlayer rotation) layered structures, as shown in Figure 1.  
38 We therefore suggest that our relatively high hydrogen gas flows allow successive h-BN  
39 layers to form below the existing layers where they align to the metal resulting in Bernal-  
40  
41  
42  
43  
44  
45  
46  
47  
48  
49  
50  
51  
52  
53  
54  
55  
56  
57  
58  
59  
60

1  
2  
3 stacked h-BN. Since this process relies on the metal only to serve as a catalyst and  
4 alignment template, other metal catalysts used for h-BN CVD beyond Fe and Cu (such as  
5 Ni, Pt, Rh, or Ir) may also support the growth of Bernal stacked h-BN.<sup>59-62</sup>  
6  
7

8  
9  
10 We note that this growth mechanism suggests that we could grow heterostructures  
11 of different materials with aligned stacking or single crystals with arbitrary twist angles  
12 by similar processes. By changing the precursor during the growth, the composition of  
13 the under-layer could be changed. By inducing nucleation at the grain boundaries of a  
14 polycrystalline metals, the orientation of the under-layer could be tuned.  
15  
16  
17  
18  
19  
20

## 21 **Acknowledgments**

22  
23  
24 This research was supported by the Director, Office of Science, Office of Basic  
25 Energy Sciences, Materials Sciences and Engineering Division, of the U.S. Department  
26 of Energy under Contract No. DE-AC02-05-CH11231, primarily within the sp<sup>2</sup>-Bonded  
27 Materials Program (KC-2207) which provided for growth of the h-BN and theoretical  
28 analysis; and in part by the van der Waals Heterostructures program (KCWF16) which  
29 provided for diffraction analysis. This work was additionally supported by the National  
30 Science Foundation under Grant # DMR-1206512 which provided for conventional TEM  
31 imaging; under Grant #1542741 which provided for construction of the LP-CVD  
32 synthesis system; and Grant #DMR 1508412 which provided for theoretical calculations.  
33 High-resolution TEM imaging at the Molecular Foundry was supported by the Office of  
34 Science, Office of Basic Energy Sciences, of the US Department of Energy under  
35 Contract No. DE-AC02-05CH11231. SMG acknowledges support from a Kavli Energy  
36 Nano Sciences Institute Fellowship and an NSF Graduate Fellowship.  
37  
38  
39  
40  
41  
42  
43  
44  
45  
46  
47  
48  
49  
50  
51  
52  
53  
54  
55  
56  
57  
58  
59  
60

	Energy (meV per cell)	Method	AA	AA'	AB	AB1'	AB2'
<b>bulk</b>	Present	GGA+TS vdW	48	$\equiv 0$	-3	5	42
	Liu (2003) <sup>23</sup>	LDA	56	0	0	8	48
	Ooi (2006) <sup>22</sup>	LDA	51	0	6	25	48
	Hu (2011) <sup>24</sup>	LDA	52	0	-2	6	47
	Constantinescu (2013) <sup>25</sup>	LMP2	80	0	3	25	82
<b>bilayer</b>	Present	GGA+TS vdW	21	$\equiv 0$	-2	2	18
	Riberio (2011) <sup>26</sup>	GGA	13	0	0	3	10
	Constantinescu (2013) <sup>25</sup>	LMP2	40	0	0	9	33
	Fujimoto (2016) <sup>27</sup>	LDA	24	0	-2	2	22

**Table A:** Computed total energies of the five high-symmetry stackings of hexagonal BN in its bulk and bilayer forms. In the present work, we use density functional theory (DFT) with the Perdew-Burke-Ernzerhof generalized gradient approximation (PBE GGA)<sup>37</sup> and norm-conserving pseudopotentials. To include the interlayer van der Waals (vdW) interactions, we have used the Tkatchenko-Scheffler (TS) correction as described in the supplement. Energies are referenced to the commonly known AA' stacking, and are in meV per unit cell (two B and two N atoms).

	Band gap (eV)	Method	AA	AA'	AB	AB1'	AB2'
<b>bulk</b>	Present	GGA+TS vdW	3.7248 (d)	4.2932 (i)	4.3751 (i)	3.6470 (i)	3.6245 (i)
	Liu (2003) <sup>23</sup>	LDA	3.226 (i)	4.027 (i)	4.208 (i)	3.395 (d)	3.433 (i)
	Ooi (2006) <sup>22</sup>	GGA	3.12 (d)	4.28 (i)	4.39 (i)	3.66 (i)	3.23 (i)
	Hu (2011) <sup>24</sup>	LDA	3.352 (i)	4.015 (i)	4.202 (i)	3.407 (i)	3.369 (i)
	Hu (2012) <sup>28</sup>	GW	4.96	5.73	5.87	5.01	4.96

<b>bilayer</b>	Present	GGA+TS vdW	4.1986 (d)	4.5249 (i)	4.5032 (i)	4.1432 (d)	4.2569 (i)
	Riberio (2011) <sup>26</sup>	GGA	4.23	4.69	4.60	4.29	4.52
	Fujimoto (2016) <sup>27</sup>	LDA	4.05 (d)	4.34 (i)	4.36 (i)	4.01 (d)	4.08 (i)

**Table B:** Electronic band gaps for hexagonal BN in its five high-symmetry stackings, listed for the bulk and bilayer cases. Indirect and direct band gaps are denoted by “(i)” and “(d)”, respectively.

		AA	AA'	AB	AB1'	AB2'	AA' [Laturia2018] <sup>31</sup>
$\epsilon_{  ,\infty}$	Bulk	4.41	4.71	4.80	4.78	4.49	4.98
	bilayer	4.40	4.68	4.74	4.75	4.43	4.97
$\epsilon_{  ,0}$	bulk	6.58	6.88	6.96	6.95	6.53	6.93
	bilayer	6.41	6.87	6.95	6.95	6.45	6.86
$\epsilon_{\perp,\infty}$	bulk	2.28	2.64	2.66	2.61	2.30	3.03
	bilayer	2.27	2.61	2.66	2.60	2.29	2.91
$\epsilon_{\perp,0}$	bulk	2.80	3.17	3.15	3.02	2.59	3.76
	bilayer	2.54	3.07	3.12	3.00	2.57	3.44

**Table C:** The high frequency (clamped-ion) and low frequency (free-ion) dielectric tensor elements for the five high-symmetry stackings of hexagonal BN. The values are relative to vacuum permittivity ( $\epsilon_{\text{vacuum}}=1$ ).



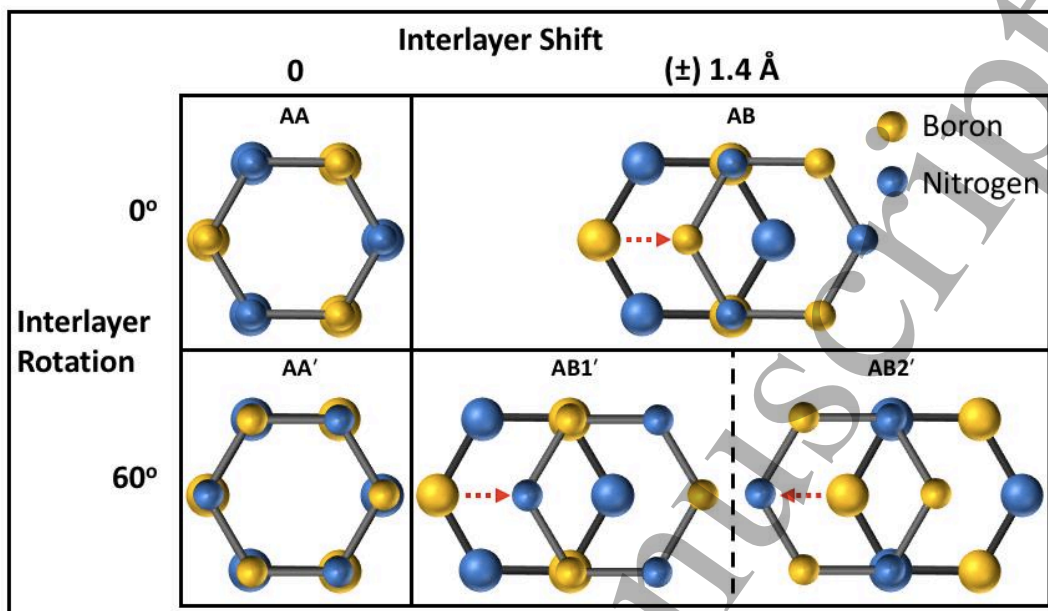


**Figure 1:** Schematics of the 5 high-symmetry stackings in bilayer h-BN as sorted by interlayer rotation and shift. In the top half of the figure, the rotationally aligned stacking configurations, AA and AB, are shown. AA is formed by stacking B to B and N to N in two aligned layers. AB is formed by translating one layer by a single bond length ( $1.4 \text{ \AA}$ )<sup>20</sup> to stack N to B as shown by the red arrow. In the bottom half of the figure, the rotationally anti-aligned stacking configurations, AA', AB1', and AB2', are shown. AA' is formed by stacking two anti-aligned layers B to N and N to B. AB1' is formed by translating one layer such that the layers stack B to B while AB2' is formed by translating one layer such that they stack N to N.

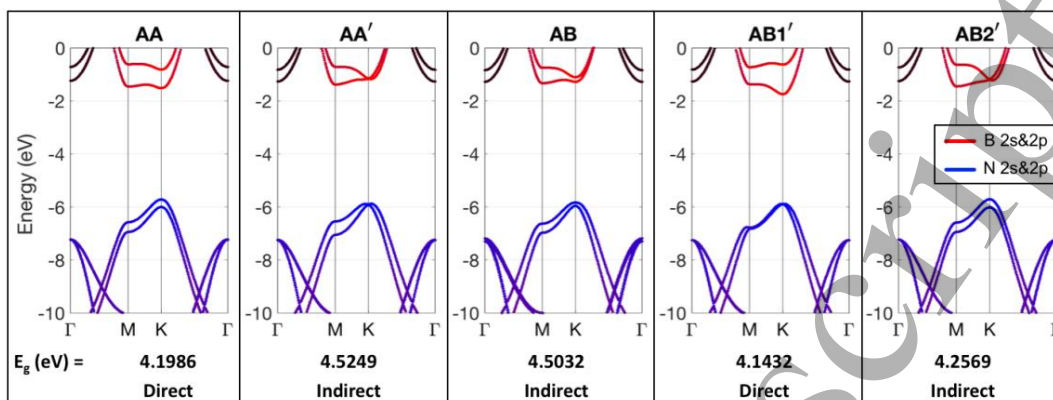


**Figure 2:** The electronic structure and bandgaps of the five physically distinct high-symmetry stackings of bilayer hexagonal boron nitride: AA, AA', AB, AB1', and AB2', from left to right. The red (blue) coloring of a band indicates the boron (nitrogen) 2s or 2p character of that band.

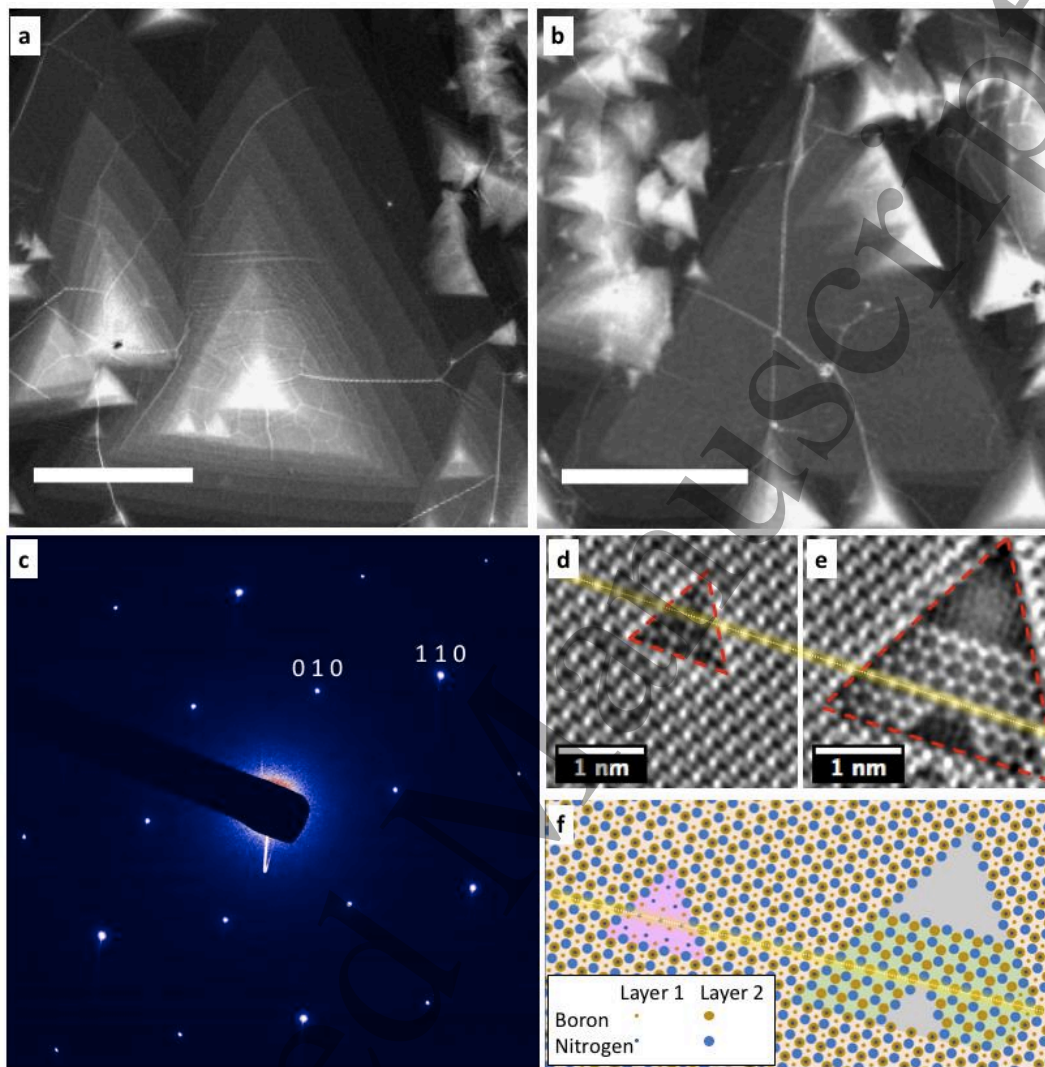
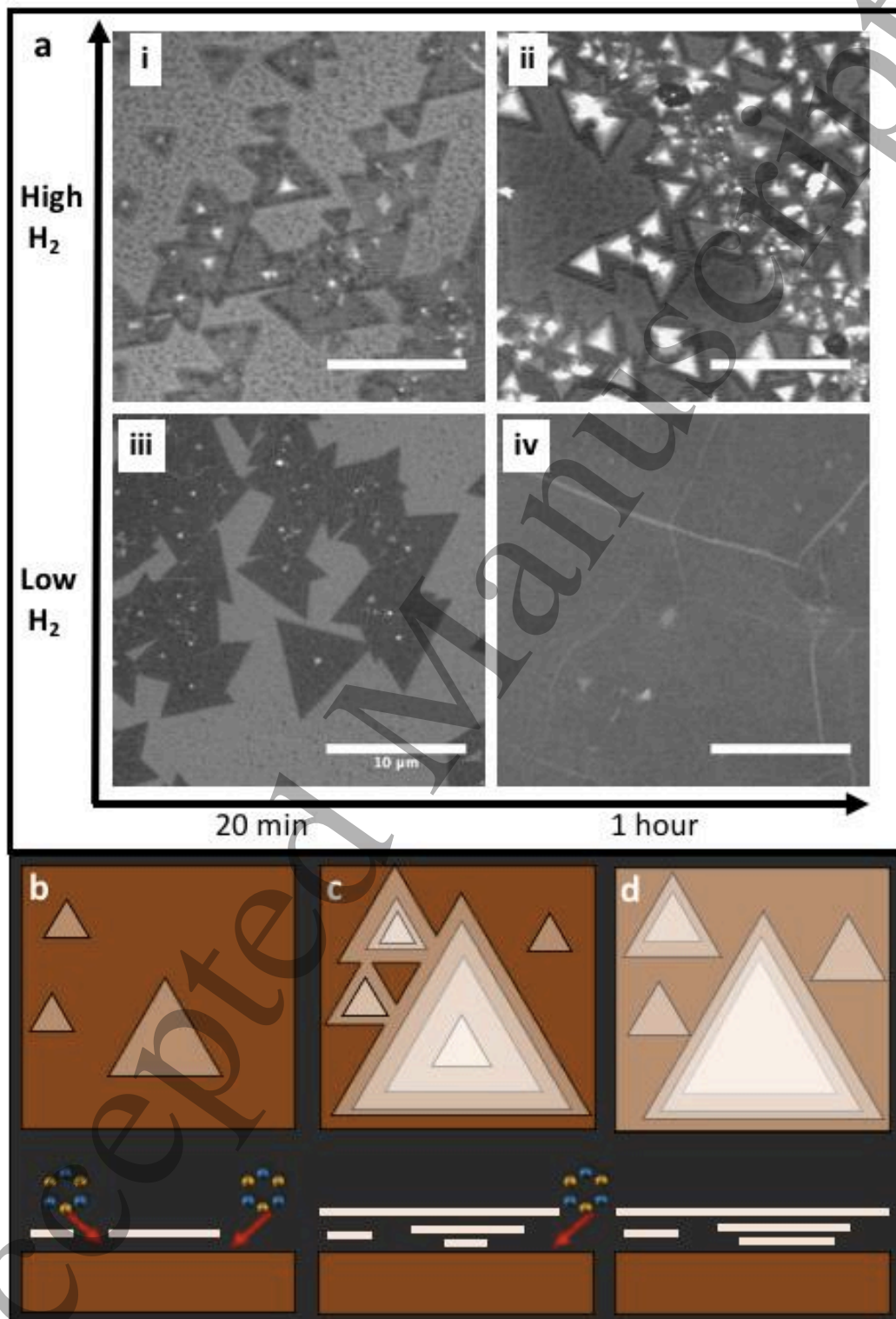


**Figure 3:** (a,b) SEM images of multilayer h-BN crystals as-grown on iron foil for 1 hour under 100 sccm  $H_2$ . The h-BN single crystals are bright contrasted triangles on a dark background of iron. Concentric triangles are additional layers stacked together. Brighter contrast indicates additional layers. (a) shows  $>10$  separate layers stacked together with a large variation in width (2-30  $\mu m$ ) while (b) shows a more continuous region of multilayer h-BN over  $\sim 40 \mu m$  that is surrounded by smaller thicker h-BN triangles. (c) A representative SAED pattern for a thick region of multilayer LP-CVD h-BN. The ratio of

1  
2  
3 the intensities of the first-order  $\langle 010 \rangle$  and second order  $\langle 110 \rangle$  peaks are compared to  
4  
5 determine the stacking order of the h-BN. The ratio of  $\sim 0.3$  as shown in Fig. S2 suggests  
6  
7 that the stacking is AB, AB1', or AB2'. (d,e) Aberration corrected HR-TEM focal series  
8  
9 reconstruction of two nearby mixed bilayer/monolayer regions of h-BN as cropped from  
10  
11 the full image shown in Fig. S3. The red-dashed triangles denote the boundary between  
12  
13 the monolayer/vacuum(inner) and the bilayer(outer) areas. (f) A schematic of the position  
14  
15 of each atom in (d,e). The atomic positions are deduced as described in the text. The  
16  
17 opaque yellow lines in (d,e,f) trace the line of stacked atoms in the bilayer region to  
18  
19 highlight the alignment of the left and right monolayer regions. Scale bars are (a)  $10 \mu\text{m}$   
20  
21 and (b)  $15 \mu\text{m}$ .  
22  
23  
24  
25  
26  
27  
28  
29  
30  
31  
32  
33  
34  
35  
36  
37  
38  
39  
40  
41  
42  
43  
44  
45  
46  
47  
48  
49  
50  
51  
52  
53  
54  
55  
56  
57  
58  
59  
60

1  
2  
3  
4  
5  
6  
7  
8  
9  
10  
11  
12  
13  
14  
15  
16  
17  
18  
19  
20  
21  
22  
23  
24  
25  
26  
27  
28  
29  
30  
31  
32  
33  
34  
35  
36  
37  
38  
39  
40  
41  
42  
43  
44  
45  
46  
47  
48  
49  
50  
51  
52  
53  
54  
55  
56  
57  
58  
59  
60



1  
2  
3 **Figure 4:** (a) SEM images of multilayer h-BN crystals grown on copper with varying  
4 times (20 min and 1 hour) and hydrogen flows (20 sccm and 200 sccm). (i) shows 3  $\mu\text{m}$   
5 triangular h-BN domains with small ad-layers (white) that are representative of a 20  
6 minute growth with 200 sccm H<sub>2</sub>. (ii) shows that after 2 hours the ad-layers grow larger  
7 while the monolayer h-BN triangle remains a similar size under 200 sccm H<sub>2</sub>. (iii) shows  
8 5  $\mu\text{m}$  triangular h-BN domains that are representative of a 20 minute growth with 20  
9 sccm H<sub>2</sub>. (iv) shows that after one hour with 20 sccm H<sub>2</sub>, the h-BN crystals merge to a  
10 full-coverage film with only minimal multi-layer coverage. (b-d) A cartoon illustrating  
11 the growth mechanism for Bernal-stacked h-BN from the top-view (above) and the side-  
12 view (below). (b) depicts the seeding and growth of h-BN monolayers. (c) shows the  
13 growth of the h-BN monolayers and the seeding of ad-layers underneath the original  
14 monolayer. (d) shows the h-BN film achieving full coverage thereby stopping the growth.  
15  
16  
17  
18  
19  
20  
21  
22  
23  
24  
25  
26  
27  
28  
29  
30  
31 Scale bars are 10  $\mu\text{m}$ .

## References

- <sup>1</sup> A.K. Geim and I. V. Grigorieva, *Nature* **499**, 419 (2013).
- <sup>2</sup> Y. Liu, N.O. Weiss, X. Duan, H.-C. Cheng, Y. Huang, and X. Duan, *Nat. Rev. Mater.* **1**, 16042 (2016).
- <sup>3</sup> F. Pizzocchero, L. Gammelgaard, B.S. Jessen, J.M. Caridad, L. Wang, J. Hone, P. Bøggild, and T.J. Booth, *Nat. Commun.* **7**, 11894 (2016).
- <sup>4</sup> J.H. Warner, M.H. Rummeli, A. Bachmatiuk, and B. Büchner, *ACS Nano* **4**, 1299 (2010).
- <sup>5</sup> D. Pacilé, J.C. Meyer, Ç.Ö. Girit, and A. Zettl, *Appl. Phys. Lett.* **92**, 133107 (2008).
- <sup>6</sup> C.R. Dean, A.F. Young, I. Meric, C. Lee, L. Wang, S. Sorgenfrei, K. Watanabe, T. Taniguchi, P. Kim, K.L. Shepard, and J. Hone, *Nat. Nanotechnol.* **5**, 722 (2010).
- <sup>7</sup> W. Gannett, W. Regan, K. Watanabe, T. Taniguchi, M.F. Crommie, and A. Zettl, *Appl. Phys. Lett.* **98**, 242105 (2011).
- <sup>8</sup> K.S. Novoselov, A.K. Geim, S. V Morozov, D. Jiang, Y. Zhang, S. V Dubonos, I. V Grigorieva, and A.A. Firsov, *Science* **306**, 666 (2004).
- <sup>9</sup> Y. Cao, V. Fatemi, S. Fang, K. Watanabe, T. Taniguchi, E. Kaxiras, and P. Jarillo-Herrero, *Nature* **556**, 43 (2018).
- <sup>10</sup> R. Ribeiro-Palau, C. Zhang, K. Watanabe, T. Taniguchi, J. Hone, and C.R. Dean, *Science (80-. )*. **361**, 690 (2018).
- <sup>11</sup> N. Marom, J. Bernstein, J. Garel, A. Tkatchenko, E. Joselevich, L. Kronik, and O. Hod, *Phys. Rev. Lett.* **105**, 46801 (2010).
- <sup>12</sup> C.-J. Kim, L. Brown, M.W. Graham, R. Hovden, R.W. Havener, P.L. McEuen, D.A. Muller, and J. Park, *Nano Lett.* **13**, 5660 (2013).

- 1  
2  
3 <sup>13</sup> R.R. Haering, *Can. J. Phys.* **36**, 352 (1958).  
4  
5 <sup>14</sup> J.-C. Charlier, X. Gonze, and J.-P. Michenaud, *Carbon N. Y.* **32**, 289 (1994).  
6  
7 <sup>15</sup> R.T. Paine and C.K. Narula, *Chem. Rev.* **90**, 73 (1990).  
8  
9 <sup>16</sup> Y. Kubota, K. Watanabe, O. Tsuda, and T. Taniguchi, *Science* **317**, 932 (2007).  
10  
11 <sup>17</sup> K.K. Kim, A. Hsu, X. Jia, S.M. Kim, Y. Shi, M. Hofmann, D. Nezich, J.F. Rodriguez-  
12 Nieva, M. Dresselhaus, T. Palacios, and J. Kong, *Nano Lett.* **12**, 161 (2012).  
13  
14 <sup>18</sup> R.S. PEASE, *Nature* **165**, 722 (1950).  
15  
16 <sup>19</sup> S.M. Kim, A. Hsu, M.H. Park, S.H. Chae, S.J. Yun, J.S. Lee, D.-H. Cho, W. Fang, C.  
17 Lee, T. Palacios, M. Dresselhaus, K.K. Kim, Y.H. Lee, and J. Kong, *Nat. Commun.* **6**,  
18 8662 (2015).  
19  
20 <sup>20</sup> N. Alem, R. Erni, C. Kisielowski, M.D. Rossell, W. Gannett, and A. Zettl, *Phys. Rev.*  
21 *B* **80**, 155425 (2009).  
22  
23 <sup>21</sup> J.D. Bernal, *Proc. R. Soc. A Math. Phys. Eng. Sci.* **106**, 749 (1924).  
24  
25 <sup>22</sup> N. Ooi, A. Rairkar, L. Lindsley, and J.B. Adams, *J. Phys. Condens. Matter* **18**, 97  
26 (2006).  
27  
28 <sup>23</sup> L. Liu, Y.P. Feng, and Z.X. Shen, *Phys. Rev. B* **68**, 104102 (2003).  
29  
30 <sup>24</sup> M.L. Hu, J.L. Yin, C.X. Zhang, Z. Yu, and L.Z. Sun, *J. Appl. Phys.* **109**, 73708 (2011).  
31  
32 <sup>25</sup> G. Constantinescu, A. Kuc, and T. Heine, *Phys. Rev. Lett.* **111**, 36104 (2013).  
33  
34 <sup>26</sup> R.M. Ribeiro and N.M.R. Peres, *Phys. Rev. B* **83**, 235312 (2011).  
35  
36 <sup>27</sup> Y. Fujimoto and S. Saito, *Phys. Rev. B* **94**, 245427 (2016).  
37  
38 <sup>28</sup> M.L. Hu, Z. Yu, J.L. Yin, C.X. Zhang, and L.Z. Sun, *Comput. Mater. Sci.* **54**, 165  
39 (2012).  
40  
41 <sup>29</sup> S. Baroni, S. de Gironcoli, A. Dal Corso, and P. Giannozzi, *Rev. Mod. Phys.* **73**, 515  
42  
43  
44  
45  
46  
47  
48  
49  
50  
51  
52  
53  
54  
55  
56  
57  
58  
59  
60



1  
2  
3 (2001).  
4

5  
6 <sup>30</sup> X. Wu, D. Vanderbilt, and D.R. Hamann, *Phys. Rev. B* **72**, 35105 (2005).  
7

8  
9 <sup>31</sup> A. Laturia, M.L. Van de Put, and W.G. Vandenberghe, *Npj 2D Mater. Appl.* **2**, 6  
10 (2018).  
11

12  
13 <sup>32</sup> R. Haubner, M. Wilhelm, R. Weissenbacher, and B. Lux, in (Springer, Berlin,  
14 Heidelberg, 2002), pp. 1–45.  
15

16  
17 <sup>33</sup> W.H. Balmain, *J. Für Prakt. Chemie* **27**, 422 (1842).  
18

19  
20 <sup>34</sup> X. Zhai and G. Jin, *J. Phys. Condens. Matter* **26**, 15304 (2014).  
21

22  
23 <sup>35</sup> C.-J. Kim, L. Brown, M.W. Graham, R. Hovden, R.W. Havener, P.L. McEuen, D.A.  
24 Muller, and J. Park, *Nano Lett.* **13**, 5660 (2013).  
25

26  
27 <sup>36</sup> W. Aggoune, C. Cocchi, D. Nabok, K. Rezouali, M.A. Belkhir, and C. Draxl, *Phys.*  
28 *Rev. B* **97**, 241114 (2018).  
29

30  
31 <sup>37</sup> Y. Ji, B. Calderon, Y. Han, P. Cueva, N.R. Jungwirth, H.A. Alsalman, J. Hwang, G.D.  
32 Fuchs, D.A. Muller, and M.G. Spencer, *ACS Nano* **11**, 12057 (2017).  
33

34  
35 <sup>38</sup> J.H. Warner, M.H. Rummeli, A. Bachmatiuk, and B. Büchner, *ACS Nano* **4**, 1299  
36 (2010).  
37

38  
39 <sup>39</sup> M.H. Khan, G. Casillas, D.R.G. Mitchell, H.K. Liu, L. Jiang, and Z. Huang, *Nanoscale*  
40 **8**, 15926 (2016).  
41

42  
43 <sup>40</sup> S.M. Gilbert, G. Dunn, A. Azizi, T. Pham, B. Shevitski, E. Dimitrov, S. Liu, S. Aloni,  
44 and A. Zettl, *Sci. Rep.* **7**, 15096 (2017).  
45

46  
47 <sup>41</sup> S.M. Gilbert, S. Liu, G. Schumm, and A. Zettl, in *MRS Adv.* (2018).  
48

49  
50 <sup>42</sup> L. Wang, B. Wu, L. Jiang, J. Chen, Y. Li, W. Guo, P. Hu, and Y. Liu, *Adv. Mater.* **27**,  
51 4858 (2015).  
52  
53  
54  
55  
56  
57  
58  
59  
60

- 1  
2  
3 43 Y. Ji, B. Calderon, Y. Han, P. Cueva, N.R. Jungwirth, H.A. Alsalman, J. Hwang, G.D.  
4 Fuchs, D.A. Muller, and M.G. Spencer, ACS Nano **11**, 12057 (2017).  
5  
6  
7 44 L. Song, L. Ci, H. Lu, P.B. Sorokin, C. Jin, J. Ni, A.G. Kvashnin, D.G. Kvashnin, J.  
8 Lou, B.I. Yakobson, and P.M. Ajayan, Nano Lett. **10**, 3209 (2010).  
9  
10  
11 45 K. Yan, H. Peng, Y. Zhou, H. Li, and Z. Liu, Nano Lett. **11**, 1106 (2011).  
12  
13  
14 46 B. Shevitski, M. Mecklenburg, W.A. Hubbard, E.R. White, B. Dawson, M.S. Lodge,  
15 M. Ishigami, and B.C. Regan, Phys. Rev. B **87**, 45417 (2013).  
16  
17  
18 47 J. Ping and M.S. Fuhrer, Nano Lett **12**, 26 (2012).  
19  
20  
21 48 T. Pham, A.P. Goldstein, J.P. Lewicki, S.O. Kucheyev, C. Wang, T.P. Russell, M.A.  
22 Worsley, L. Woo, W. Mickelson, and A. Zettl, Nanoscale **7**, 10449 (2015).  
23  
24  
25 49 F.H. Horn, J. Appl. Phys. **30**, 1611 (1959).  
26  
27  
28 50 T. Pham, A.L. Gibb, Z. Li, S.M. Gilbert, C. Song, S.G. Louie, and A. Zettl, Nano Lett.  
29 **16**, 7142 (2016).  
30  
31  
32 51 N. Alem, R. Erni, C. Kisielowski, M.D. Rossell, P. Hartel, B. Jiang, W. Gannett, and  
33 A. Zettl, Phys. Status Solidi - Rapid Res. Lett. **5**, 295 (2011).  
34  
35  
36 52 J. Kotakoski, C.H. Jin, O. Lehtinen, K. Suenaga, and A. V. Krasheninnikov, Phys. Rev.  
37 B **82**, 113404 (2010).  
38  
39  
40 53 C. Jin, F. Lin, K. Suenaga, and S. Iijima, Phys. Rev. Lett. **102**, 195505 (2009).  
41  
42  
43 54 P. Sutter, J. Lahiri, P. Albrecht, and E. Sutter, ACS Nano **5**, 7303 (2011).  
44  
45  
46 55 P.R. Kidambi, R. Blume, J. Kling, J.B. Wagner, C. Baetz, R.S. Weatherup, R.  
47 Schloegl, B.C. Bayer, and S. Hofmann, Chem. Mater. **26**, 6380 (2014).  
48  
49  
50 56 Q. Li, H. Chou, J.-H. Zhong, J.-Y. Liu, A. Dolocan, J. Zhang, Y. Zhou, R.S. Ruoff, S.  
51 Chen, and W. Cai, Nano Lett **13**, 41 (2013).  
52  
53  
54  
55  
56  
57  
58  
59  
60

- 1  
2  
3  
4  
5  
6  
7  
8  
9  
10  
11  
12  
13  
14  
15  
16  
17  
18  
19  
20  
21  
22  
23  
24  
25  
26  
27  
28  
29  
30  
31  
32  
33  
34  
35  
36  
37  
38  
39  
40  
41  
42  
43  
44  
45  
46  
47  
48  
49  
50  
51  
52  
53  
54  
55  
56  
57  
58  
59  
60
- <sup>57</sup> S. Nie, W. Wu, S. Xing, Q. Yu, J. Bao, S. Pei, and K.F. McCarty, *New J. Phys.* **14**, 93028 (2012).
- <sup>58</sup> Y. Yang, Q. Fu, H. Li, M. Wei, J. Xiao, W. Wei, and X. Bao, *ACS Nano* **9**, 11589 (2015).
- <sup>59</sup> R. Zhao, X. Zhao, Z. Liu, F. Ding, and Z. Liu, *Nanoscale* **9**, 3561 (2017).
- <sup>60</sup> A. Gibb, N. Alem, and A. Zettl, *Phys. Status Solidi* **250**, 2727 (2013).
- <sup>61</sup> A. Hemmi, C. Bernard, H. Cun, S. Roth, M. Klöckner, T. Kälin, M. Weinl, S. Gsell, M. Schreck, J. Osterwalder, and T. Greber, *Rev. Sci. Instrum.* **85**, 35101 (2014).
- <sup>62</sup> F. Schulz, R. Drost, S.K. Hämäläinen, T. Demonchaux, A.P. Seitsonen, and P. Liljeroth, *Phys. Rev. B* **89**, 235429 (2014).